ADSUJSR 13 (1) (2025) 01-14
Adamawa State University Journal of Scientific Research (ADSUJSR)
http://www.adsujsr.edu.ng
ISSN: 2705-1900 (Online); ISSN: 2251-0702 (Print)

PREPARATION OF BIMODAL INORGANIC UIO-66 NANOCOMPOSITE MEMBRANE VIA EX-SITU DEPOSITION FOR ENHANCED NANOFILTRATION

Shangkum Yildun Goji[a]*, Saraya Akuben Yakubu[a], Rotbe Gurumji[b], Moses Titus Yilleng[a], Ohwimu Joseph Godday[c], Muhammad Ibrahim[a], Solomon Almanto Mamuru[d]

a Department of Chemistry, Faculty of Natural Sciences, University of Jos, P.M.B 2084, Jos, Nigeria.
b Plateau State College of Agriculture, Garkawa, P.M.B 001, Mikang, Plateau State, Nigeria
c Department of Chemistry, Federal University of Petroleum Resources, Effurun, Delta State, Nigeria.
d Department of Pure and Applied Chemistry, Adamawa State University, Mubi

*Corresponding author e-mail: *gojis@unijos.edu.ng; shangkum86@gmail.com*

Received in July 2025
Accepted in August 2025

Abstract

Achieving a balance between flux and rejection remains a key challenge in nanofiltration membrane design for water treatment. In this study, a bimodal inorganic UiO-66 nanocomposite membrane was fabricated using an ex-situ deposition method and evaluated for filtering organic contaminants from water. Polydispersed UiO-66 nanoparticles (14 and 108 nm) were synthesized by modulating water content (0.2–2.0 mL) during synthesis. Characterization via XRD, TEM, FTIR, and TGA confirmed the structure and distribution of UiO-66. XRD results showed characteristic peaks at 2θ = 7.34° and 8.48°, indicating the formation of a face-centered cubic crystal structure. Peak broadening at 2θ = 8.6° and 10° was observed with increased water addition. TEM analysis revealed the impact of water modulation on nanoparticle size. Unimodal UiO-66 suspensions (14 and 108 nm) were deposited on a microfiltration regenerated cellulose (RC) support via suction filtration (900 mbar, 30 min), forming a bimodal membrane. After partial drying, the membranes were tested for methylene blue rejection. At 99% rejection and 900 mbar pressure, the bimodal UiO-66 membrane achieved a high water permeability of 400 ± 5.33 L/m²/h. These results demonstrate the potential of ex-situ synthesized bimodal UiO-66 membranes for efficient nanofiltration in water treatment.

Keywords: UiO-66 Nanocomposite, Water Purification, Nanofiltration, Control Packing. UiO-66, ex-situ deposition method, small molecules, fouling propensity.

Introduction

Membrane technology has gained significant attention in various industrial applications, including water treatment, gas separation, and biotechnology (Van der Bruggen & Vandecasteele, 2007; Nunes & Peinemann, 2010; Wijmans & Baker, 2012; Lueptow & Khinast, 2017). Among these technologies, nanofiltration (NF) membranes have become a focal point due to their ability to selectively filter out small organic molecules and ions while permitting the passage of water and larger molecules. Their superior separation efficiency, low energy consumption, and effectiveness in removing contaminants from aqueous solutions make them indispensable in

modern separation processes (Jindal et al., 2016; Li et al., 2018; Ghosh et al., 2018; Mondal & Wickramasinghe, 2019; Goh et al., 2019). Despite their advantages, challenges persist in optimizing NF membrane performance due to limitations in pore size control and surface characteristics.

Nanocomposite membranes have emerged as a promising solution, offering enhanced mechanical and thermal stability, improved permeability and selectivity, and superior resistance to fouling and chemical degradation (Li et al., 2018; Wu et al., 2019; Yang et al., 2019; Ma et al., 2020). Metal-organic frameworks (MOFs), particularly UiO-66, have garnered significant interest due to their unique structural and chemical properties. UiO-66 exhibits exceptional stability, porosity, and chemical resistance, making it an ideal candidate for incorporation into bimodal nanocomposite membranes for nanofiltration applications (Sun et al., 2017; Teng et al., 2018; Zheng et al., 2019; Su et al., 2020; Wang et al., 2021).

Recent studies have demonstrated the successful fabrication of UiO-66-based bimodal nanocomposite membranes using various deposition techniques. Moghaddam et al. (2021) reported the development of a UiO-66/polyethylene glycol (PEG)-coated polysulfone (PSf) membrane, which exhibited excellent separation efficiency for heavy metals and organic pollutants. Similarly, Huang et al. (2021) employed a thermal annealing process to enhance the separation efficiency of UiO-66-incorporated membranes for dyes and heavy metals. Deposition techniques such as layer-by-layer (LBL), dip-coating, and spin-coating have been explored to integrate UiO-66 nanoparticles into polymeric membranes, improving water flux and contaminant rejection (Zhang et al., 2018; Wang et al., 2019; Liu et al., 2019). Despite these advancements, several challenges remain in optimizing UiO-66-based bimodal nanocomposite membranes. The heterogeneous nucleation of UiO-66 crystals often leads to non-uniform barrier layers, interfacial defects, and structural disorganization, limiting membrane performance and scalability. Additionally, some deposition methods may not be suitable for applications requiring specific membrane properties, such as reverse osmosis or ultrafiltration. To address these issues, further research is required to refine fabrication techniques and evaluate membrane performance under various water treatment conditions.

This study presents an ex-situ deposition method for the preparation of a bimodal UiO-66 nanocomposite membrane, focusing on optimizing nanoparticle distribution and enhancing separation efficiency. UiO-66 nanoparticles of varying sizes were synthesized using water as a modulator and subsequently deposited onto a hydrophilic regenerated cellulose (RC) substrate. Smaller nanoparticles filled the corrugated spaces between larger particles, enabling precise control over membrane thickness and porosity. The resulting membrane exhibited high water permeability and superior methylene blue (MB) rejection due to the hydrophilic pore architecture of UiO-66. The ex-situ deposition approach offers a promising strategy for the development of high-performance NF membranes, contributing to advancements in water treatment technology.

Materials and Method

Materials

Zirconium tetrachloride ($ZrCl_4$, 99%) and terephthalic acid (99%), both of which were bought from Sigma-Aldrich Co., were the ingredients employed in the manufacture of UiO-66 nanoparticles. The support membrane, RC 58 (with a diameter of 47 mm and pore size 0.2 m), was purchased from Whatmann G.E Healthcare Germany. The solvents, N, N-dimethylformamide (DMF) and methanol (MeOH), were procured from Wako Chemical Industries Ltd. Kanto Chemical Co. Inc. supplied the methylthioninium chloride (methylene blue (MB) 98.5% purity), which was employed as the organic pollutant. The entire experiment was conducted with deionized (DI) water.

Preparation of UiO-66 Nanoparticles

The following method was used to create UiO-66 nanoparticles. In contrast, 2.28 mmol of terephthalic acid was dissolved in 30 mL of DMF to create a solution of $ZrCl_4$, which was created by combining

1.63 mmol of $ZrCl_4$ with that amount of DMF. The subsequent step was to combine the terephthalic acid solution and the $ZrCl_4$ solution in a 100 mL vial. The combination was then agitated while under a N_2 environment. The appropriate volume of DI water (2.0–0.2 mL) was then added. To produce crystalline dispersion of UiO-66 $[Zr_6O_4(OH)_4(C_8O_4H_4)_6]$ nanoparticles, the mixture was heated at 100°C for 12 hours in an oil bath with constant stirring. The created nanoparticles were gathered, and DMF three was used to repeatedly wash them. The synthesis route of UiO-66 nanoparticles is shown in **Scheme 1.**

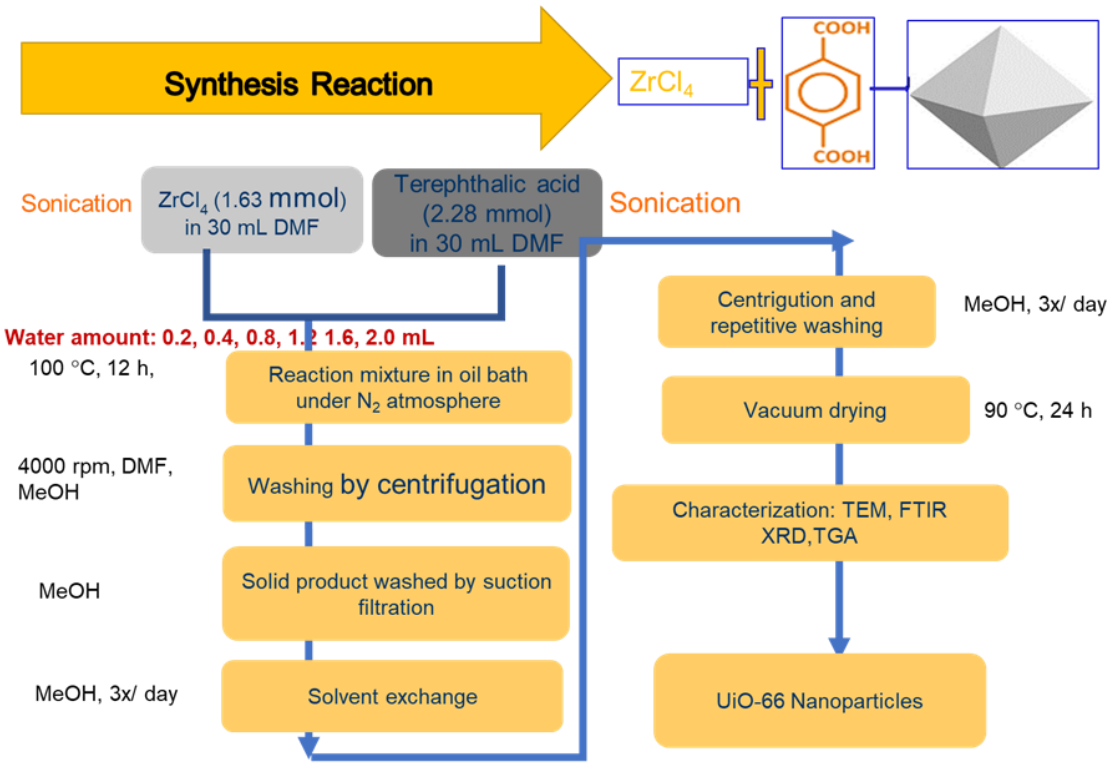

Scheme 1. Synthesis of UiO-66 nanoparticles

In Scheme 2, the process for creating UiO-66 nanocomposite membranes via deposition method and the filtering capabilities of the created nanocomposite are described.

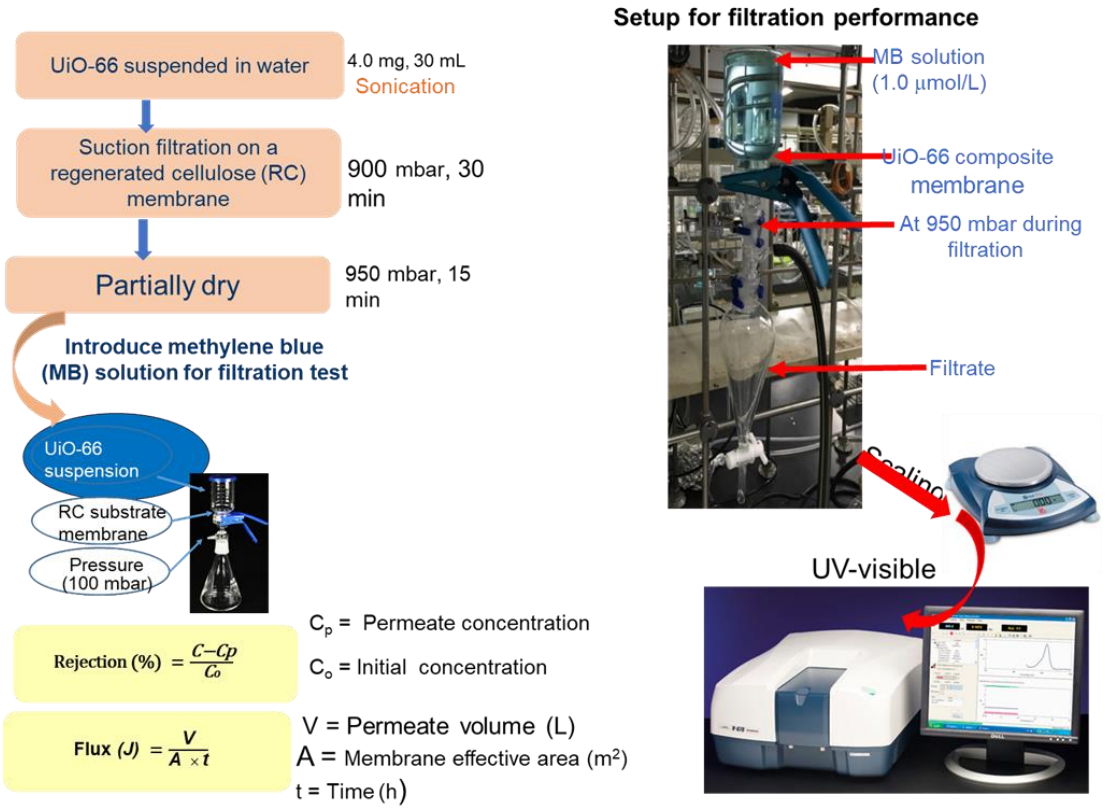

Scheme 2. UiO-66 Nanocomposite Membrane Preparation and Performance Evaluation2.3.

Characterization of UiO-66 Nanoparticles

Transmission electron microscopy (TEM, Hitachi H7100) was used to examine the morphology of UiO-66 nanoparticles at a 100 kV accelerated voltage. Using ImageJ software, the particle size was extracted from the TEM images. By employing CuK radiation at 2 = 5-35° in steps of 0.1°/150 sec., X-ray diffraction (XRD, Rigaku SmartLab) was used to examine the crystal structure of the produced UiO-66 nanoparticles. Scherrer's formula was used to determine the particles' crystalline size as seen in Eq. (1).

$$D = \frac{0.94\,\lambda}{ß\cos\theta} \qquad (1)$$

where, λ= 0.94 Å for CuKα, ß = full width at half-maximum (FWHM), θ = Bragg's angle.

The functional groups present in the synthesized UiO-66 were assessed using Fourier transform infrared spectra (FTIR) (Jasco FT/IR-6100) spectrometer in the range of 400-2400 cm1 at a resolution of 4 cm1 scans accumulation of thirty-two, while the particle size was estimated using dynamic light scattering (DLS). On a ThermoPlus EVO II (Rigaku) thermal analyzer, the thermogravimetric analysis (TGA) was carried out. Based on the weight loss between 300 and 600 °C in relation to the final residual inorganic matter, the organic matter content was calculated (ZrO2). The techniques presented in these studies were used for the fabrication, characterization, and assessment of filtration capabilities of nanocomposite membranes (Goji et al., 2018; Chen, et al., 2018; Alghunaimi, et al., 2018).

Characterization

Transmission electron microscopy (TEM) pictures showing the size and structure of the various UiO-66 nanoparticle crystals are shown in Figure 1. Using ImageJ software, the diameters of the UiO-66 nanoparticles were determined and are shown in Table 1. The polygonal cubic crystal forms of extremely small to bigger particle clusters were evident in the morphology of UiO-66 nanoparticles. The width of the various nanoparticles is the same, but their crystal lengths vary. For UiO-66, this change in crystal sizes and length correlated with the amount of additional water (14-108 nm). For instance, it was discovered that the size of the particles in which more water was added was smaller than that of the particles in which less water was added (Table 1). The polygonal cubic crystal forms of extremely small to bigger particle clusters were evident in the morphology of UiO-66 nanoparticles. The width of the various nanoparticles is the same, but their crystal lengths vary. For UiO-66, this change in crystal sizes and length correlated with the amount of additional water (14-108 nm). For instance, it was discovered that the size of the particles in which more water was added was smaller than that of the particles in which less water was added (Table 1). Also, it was noted that the synthesis of the UiO-66 crystals caused the reaction mixture to turn turbid more quickly when 2.0 mL of water was added than when only 0.2 mL of water was added. Several academics have seen and documented this similar pattern.

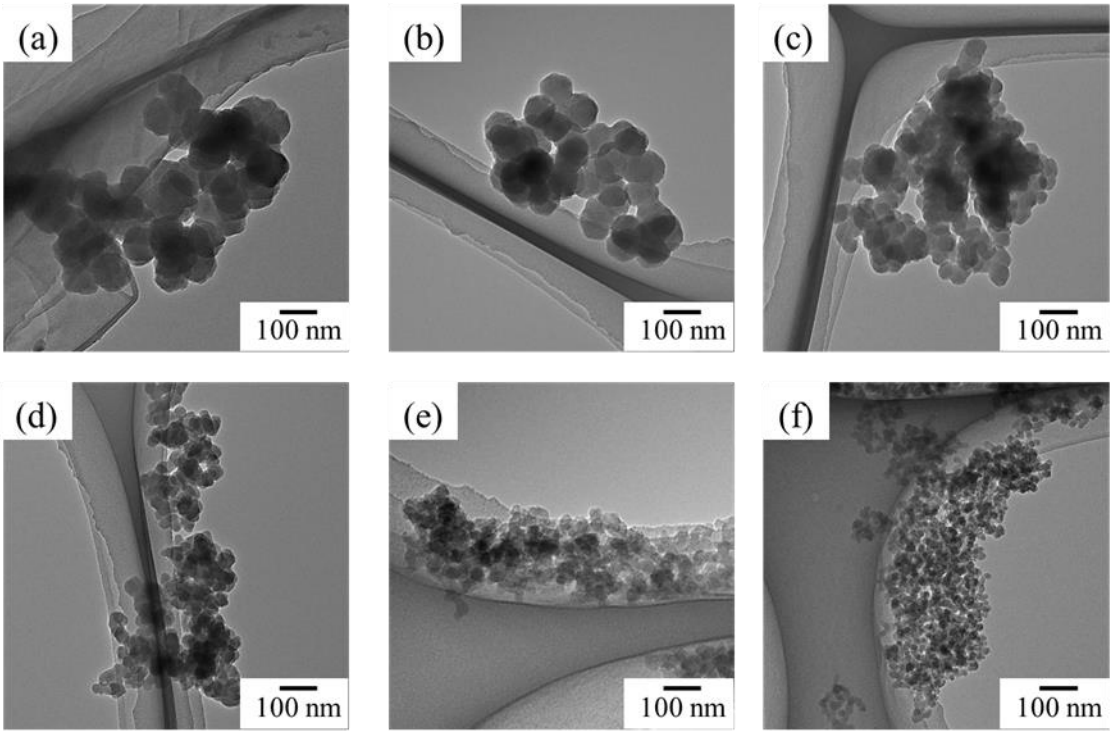

Figure 1. TEM images of UiO-66 samples: a) UiO-66 (108 nm), b) UiO-66 (88 nm), c) UiO-66 (75 nm), d) UiO-66 (23 nm), e) UiO-66 (20 nm) and f) UiO-66 (14 nm).

Dynamic light scattering (DLS)

A potent method for determining the particle size distribution of materials in solution is dynamic light scattering (DLS). It functions by detecting variations in scattered light intensity brought on by the Brownian motion of particles suspended in a liquid. The size, shape, and distribution of the particles in the suspension can be determined using the data from DLS measurements. The use of DLS in establishing the hydrodynamic radius of the particles in solution, a

crucial factor in evaluating the properties and applications of UiO-66, is of utmost relevance when estimating the average particle size of UiO-66. This DLS is a quick, non-destructive, and sensitive method for determining particle size distributions across a broad size range (Bösecke et al. (2013); Schmitt et al. (2013); Kallmes et al. (2015). DLS should be regarded as a vital analytical tool for characterizing UiO-66 and other MOFs as a result. The average frequencies as determined by dynamic light scattering were plotted against the TEM nanoparticle sizes, as shown in Figure 2. According to the graph, most suggested nanoparticle sizes fall within the range of 100 nm and 120 nm. Most UiO-66 nanoparticles that have been produced and described in the literature have also attained sizes under 100 nm. The size averages and median values in this study are 14 nm (Jeong & Joo, 2008; Sorensen, and Toney, 2013). The use of water as a modulator caused this UiO-66 MOF to exhibit size variation. The smallest measurement made this synthesis offers strategies for reducing nanocrystal sizes. In contrast, the median values showed the sizes that were most likely to be achieved when utilizing the modulation synthetic approach.

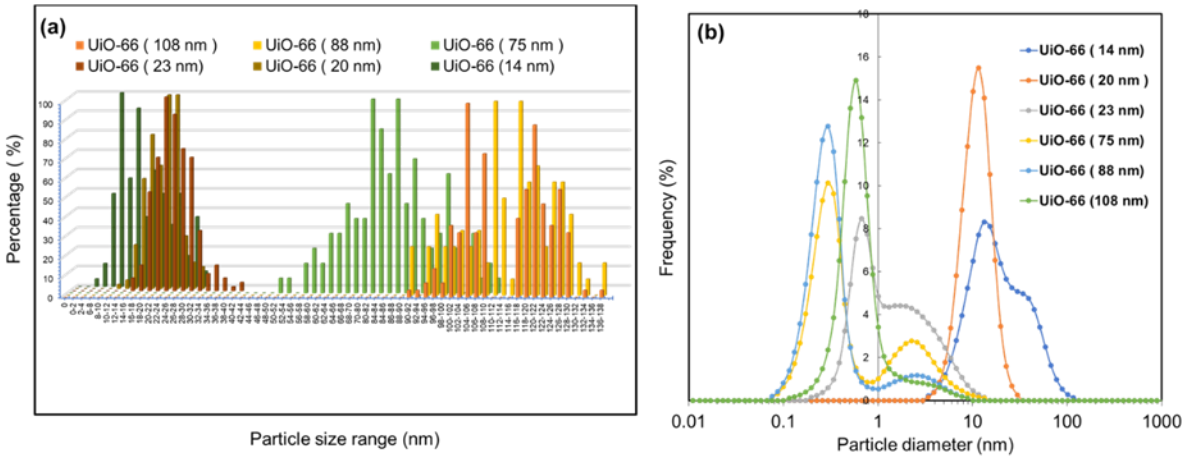

Figure 2. Particle size range and diameter obtained from a) TEM and b) Dynamic light scattering

A popular method for examining the vibrational characteristics of MOFs, including UiO-66, is Fourier transform infrared spectroscopy (FTIR). Figure 3a depicts the FTIR spectra of UiO-66 MOFs. Both the stretching vibrations of the Zr-O bonds in the inorganic nodes and the stretching vibrations of the carboxylate groups in the organic linker are responsible for the peaks in the FTIR spectrum of UiO-66 MOFs. For FTIR investigation of UiO-66 MOFs, spectra of the powdered sample are commonly obtained using a spectrophotometer with a range of 2400–400 cm-1. Following that, the acquired spectra are examined to determine which characteristic absorption bands correspond to the vibrational modes of the different chemical bonds inside the MOF. Strong absorption is one of the most noticeable characteristics of UiO-66 FTIR spectra. The acquired spectra are then examined to determine the distinctive absorption bands that match the vibrational modes of the different chemical bonds in the MOF. Strong absorption lines at 1396 cm^{-1}, which are associated with the stretching vibrations of the C=O bonds in the BDC linkers, are one of the distinguishing characteristics of UiO-66 FTIR spectra (Li, et al., 2009; Aguado, et al., 2011; Zhang, et al., 2014; DeCoste, & Peterson, 2014; Zhang, et al., 2018; Zhang, et al., 2019). The precise location and form of this band can be utilized to gauge the strength of the hydrogen bonding between the MOF's $Zr_6O_4(OH)_4$ clusters and BDC linkers. A stronger hydrogen bond is indicated by a shift to higher wavenumbers and a shortening of the band, while a shift to lower wavenumbers and a broader band indicates poorer hydrogen bonding. A sharp absorption band at around 745 cm^{-1}, which corresponds to the stretching vibrations of the Zr-O bonds in the $Zr_6O_4(OH)_4$ clusters, and peaks in the range of 400-800 cm-1, which correspond to the Zr-O vibrations in the

inorganic nodes, are present in the UiO-66 FTIR spectra (Zhang, et al., 2014; Ahmed et al., 2015; Sholl, & Lively, 2016; Liu, et al., 2016; Jana, et al., 2017). The location and intensity of this band can be utilized to track changes in the local structure of the MOF brought on by external stimuli like temperature or pressure as well as to keep track of the coordination environment of the Zr ions within the MOF. UiO-66 FTIR spectra shows additional weaker absorption bands in addition to these noticeable ones. The bending and stretching vibrations of the various functional groups in the MOF, such as the C-H, C-O, and O-H bonds in the BDC linkers and the Zr-O bonds in the $Zr_6O_4(OH)_4$ clusters, are also visible in the UiO-66 FTIR spectra in a number of weaker bands between 1091 and 1161 cm^{-1} (Valenzano, et al., 2011; Rodenas, et al., 2014; Dong, et al., 2016; Yang, et al., 2017; Hu, et al., 2019). Further details about the MOF's local structure and chemical environment can be learned from these weaker bands. Sharp diffraction peaks indicative of the (hkl) crystal planes of the cubic structure can be seen in Figure 3b XRD pattern for UiO-66. According to reports, the strongest peaks for a face-centered cubic crystal are found at 2θ = 7.34° and 8.48°, which correlate to strong (111), (002) Bragg peaks (Valenzano, et al., 2011; Chavan, et al., 2012). Yet, it was found that changing the amount of water introduced also changes the relative intensities of the Bragg peaks and the widths of the reflections. As more water was added, the widths widened, indicating the production of nanoscale crystallites. The width was narrower even though there was less water being used. It was discovered that the size of the reflections keeps growing. It was discovered that the width of the reflections increases as the water volume increases, indicating that the particles get smaller as the water level rises. Similar research was done by Wu et al., who reported that the synthesis of UiO-66 was affected by a variety of modulators, including water, and that this resulted in the production of a well-crystalline UiO-66 phase, which was supported by XRD analysis. With a lattice parameter of 25.8, the XRD pattern displayed strong peaks corresponding to the cubic UiO-66 structure, which is consistent with earlier research (Wu, et al (2012). The pattern of UiO-66 particles produced with more water was seen at an area where a broad peak covering a 9°–10° range could be seen. The missing cluster flaws' nanoregions were attributed to this broad peak. Missing cluster defects, or portions of the framework where one or more zirconium ions are missing, were found to be the cause of the broad peak in the XRD pattern of UiO-66 MOF. These defects lead to incomplete linkers and altered local coordination environments. The broad peak shown in the XRD pattern, which is indicative of the short-range disorder in the framework, has been postulated to be caused by the nanoregions of missing cluster defects. It has been demonstrated that the synthesis circumstances, including the modulator utilized and the reaction temperature, affect the level of disorder and the strength of the broad peak (Demessence, et al., 2009; Planas, et al., 2013; Shearer, et al., 2014). The amount of water injected during the synthesis process was associated with the relative strength of the broad peak. Scherrer's equation was used to get the crystallite diameters, which are shown in Table 1. Also, it was noted that the broadness of the peaks indicates that the addition of water resulted in the production of smaller crystal particles. According to the results of these studies on synthetic reactions, the kinetics of crystallization and crystallite size can be systematically controlled by varying the amount of water added during the synthesis, which is consistent with work of a similar nature that has been published by other researchers using water as a solvent (Eddaoudi, et al., 2002; Farha, et al.,2009; Li, et al., 2009; Li & Zhou, 2010; Kreno, et al., 2012; Liu, et al., 2016; Zhang, et al.,2018).

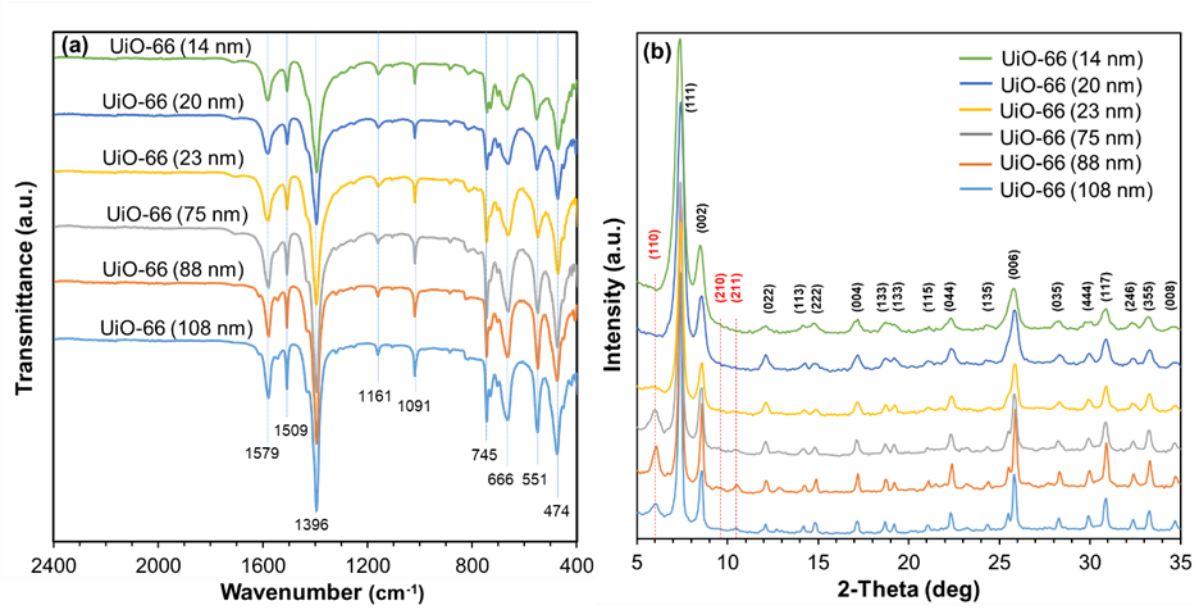

Figure 3. (a) FT-IR spectrum of UiO-66 samples and (b) XRD patterns.

Thermogravimetric analysis

To check the thermal stability of UiO-66 samples, thermogravimetric analysis (TGA) was performed. The TGA is an accessible method that can provide information on how to assess the presence of defects in the sample. The organic contents of the UiO-66 nanoparticle were determined based on weight loss between 200 and 600 °C. The TGA analysis for UiO-66 (14 nm–108 nm) is as presented in Table 1. The theoretical content of organic matter for a perfect inorganic framework is expected to be 59.17. This is because an ideal UiO-66 framework is built up of $[Zr_6O_4(OH)_4]$ clusters, which are interconnected by a maximum of 12 linkers (Valenzano et al., 2011; Haldoupis, et al., 2013; Eddaoudi, et al., 2002; Tranchemontagne, et al., 2008; Cavka, et al.,2008). Therefore, it is expected that the final weight loss in relation to the theoretical value should be similar among the samples. The organic content of the UiO-66 (14 nm–23 nm) samples, as shown in Table 1, shows that the weight losses are close in the case of UiO-66 (75 nm) and UiO-66 (88 nm). Furthermore, it was also observed that the organic contents fell significantly short of the theoretical weight, which implies that the frameworks of the synthesized UiO-66 nanoparticles were lighter than the ideal framework. Therefore, based on the TGA data obtained, it was estimated that some linkers were inherently missing at each cluster for these two samples, and the ratio of linker to the Zr cluster in these samples was found to be 8.0 in the case of UiO-66 (88 nm) and 9.0 for UiO-108 nm. This lower content could be due to missing linkers because of the slow reaction kinetics of Zr salt with the sample's linker where a small amount of water was added to the reaction system resulting in incomplete crystallization and thus a defective structure (Tranchemontagne, et al., 2008; Duan, et al., 2018). As such, it was concluded that UiO-66 (88 nm) and UiO-66 (108 nm) possess defective structures resulting from the linkers deficiency.

As shown in Table 1, the crystal growth rate was found to be dependent on the amount of water that was added to reaction system. Therefore, we concluded that by regulating this variable, the particle sizes were successfully tailored.

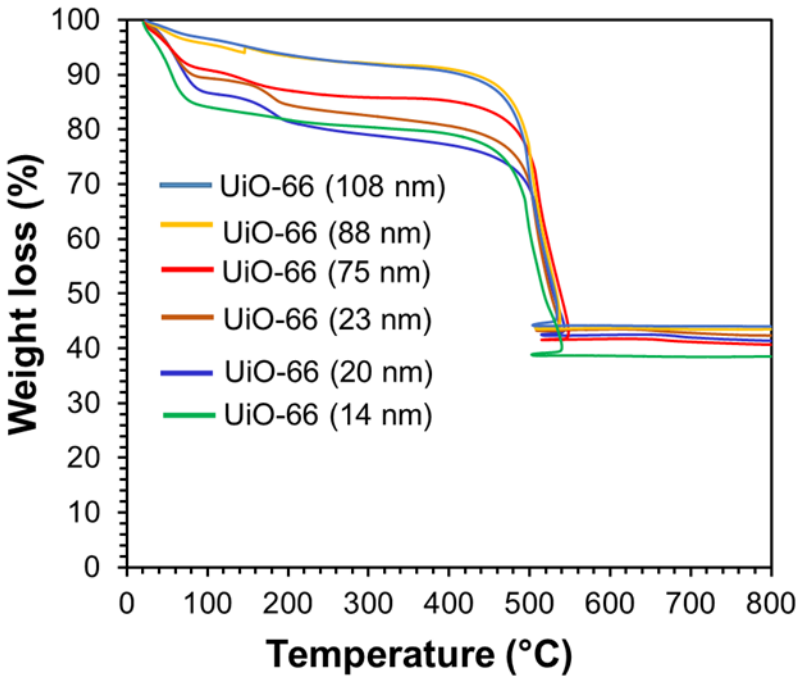

Figure 4. Thermogravimetric profile of UiO-66 (14 nm) - UiO-66 (108 nm)

Deposition of UiO-66 Nanoparticle on Regenerated Cellulose

Pre-formed UiO-66 nanoparticles with varying particle sizes (14 nm and 108 nm) were used to create a variety of MOF composite membranes. Since water is more affordable and environmentally friendly than solvents like DMF or DMA, which are harsh and can deteriorate polymeric substrates in addition to intensifying the washing of the composite membrane after deposition, these solvents were chosen as the dispersion medium for the membrane. When less water is used during membrane preparation, washing processes are also reduced. The regenerated cellulose support membrane was coated with UiO-66 nanoparticles that had been suspended in water, sonicated, suction filtered and allowed to dry to create a composite membrane. The SEM images in **Figure 5a-f** show the cross-sectional images of the composite membrane prepared from UiO-66 (14 nm–108 nm) and that of the RC. It can be clearly seen that the deposited layer exhibits a different morphology from that of the support membrane. However, SEM of the RC support membrane displayed a highly porous morphology with many cellulose fibers disorderly intertwined among each other, whereas the structure of the composite membranes showed morphologies of the subcutaneous layer of UiO-66 nanoparticles homogeneously packed on the support membrane. The cross-sectional images show excellent attachment between UiO-66 and the support material. The shape of the UiO-66 samples produced may have contributed to the agglomeration of the particles and intergrowth of larger aggregates than the single crystal seen in the TEM pictures. So, it's possible that during the deposition stage, these aggregates quickly filled the membrane's pores.

Both during the fabrication of the membrane and the filtration exercise, we noticed that no nanoparticles passed through the RC membrane and into the permeate

.

Table 1. Preparation conditions, particle characteristics, and the organic content of UiO-66 samples

Sample	Water Amount[a] (mL)	Particle Size [b] from TEM (mL)	Crystallite Size[c] from XRD (nm)	Organic content[d] (wt. %)	Ligand per[e] $Zr_6O_4(OH)_4$ Cluster
UiO-66 (14 nm)	2.0	14	25 (18)	56.18	11
UiO-66 (20 nm)	1.6	20	37 (21)	53.94	10
UiO-66 (23 nm)	1.2	23	42 (28)	53.66	10
UiO-66 (75 nm)	0.8	75	46 (37)	53.19	10
UiO-66 (88 nm)	0.4	88	66 (51)	48.39	8
UiO-66(108 nm)	0.2	108	83 (52)	48.94	9

[a]Water amount added during the synthesis of UiO-66 (14 nm- 108 nm), [b] Median particle size (number base) acquired from TEM image using the ImageJ software, [c] determined using the Scherrer equation for (002) plane, while the [d] determined based weight loss between 200-600 °C in the TGA analysis. The reported values are the weight loss between 300-600◦C with respect to ZrO_2 as final residual product

The cross-section of the SEM clearly demonstrates a densely packed UiO-66 subcutaneous layer with a range of particle sizes on the substrate's surface. The composite membrane's top-view picture (Figure 5f) demonstrates homogeneous UiO-66 coverage across the entire substrate and on the porous RC substrate, a continuous layer of nanoparticles made of crack-free UiO-66 particles This demonstrated the UiO-66 nanoparticles' strong chemical interaction with water, which served as an environmentally friendly dispersion medium, and their adhesion to the surface of the RC substrate membrane. As a result, the membrane stability was increased, demonstrating the success of the fabrication of a selective layer of UiO-66 nanoparticles-deposited composite membrane.

Figure 6a to e displays the cross-sectional SEM images of the UiO-66 particles at various sizes: 14 nm, 20 nm, 23 nm, 75 nm, 88 nm, and 108 nm. To create space and voids within themselves, UiO-66 crystals were equally dispersed and stuck to the RC fibers, resulting in high coverage of the substrate surface as seen in the SEM images. Since their number and size tend to increase with increasing particle size, it was shown that these voids are related to the range of particle sizes. Thus, we assume that the UiO-66 particles may have been scattered throughout the substrate's surface without entering the pores.

Figure 7 displays a magnified cross-sectional SEM picture of the UiO-66 (108 nm) composite membrane under various loading conditions. It is evident that as the loading of the nanoparticles increased, the deposition layer's thickness changed. The selective layer of the UiO-66, which has nanopores with a size of 6 nm, the nanosize, and partially the loading/deposition layer of the nanoparticles were the main causes of the sieving ability of these nanoparticles during filtering. When 1.0 mg, 3.0 mg, and 4.0 mg of the nanoparticles were deposited on the RC substrate, respectively, it was discovered that the thickness of the particles was 1.5 m, 4 m, and 6 m.

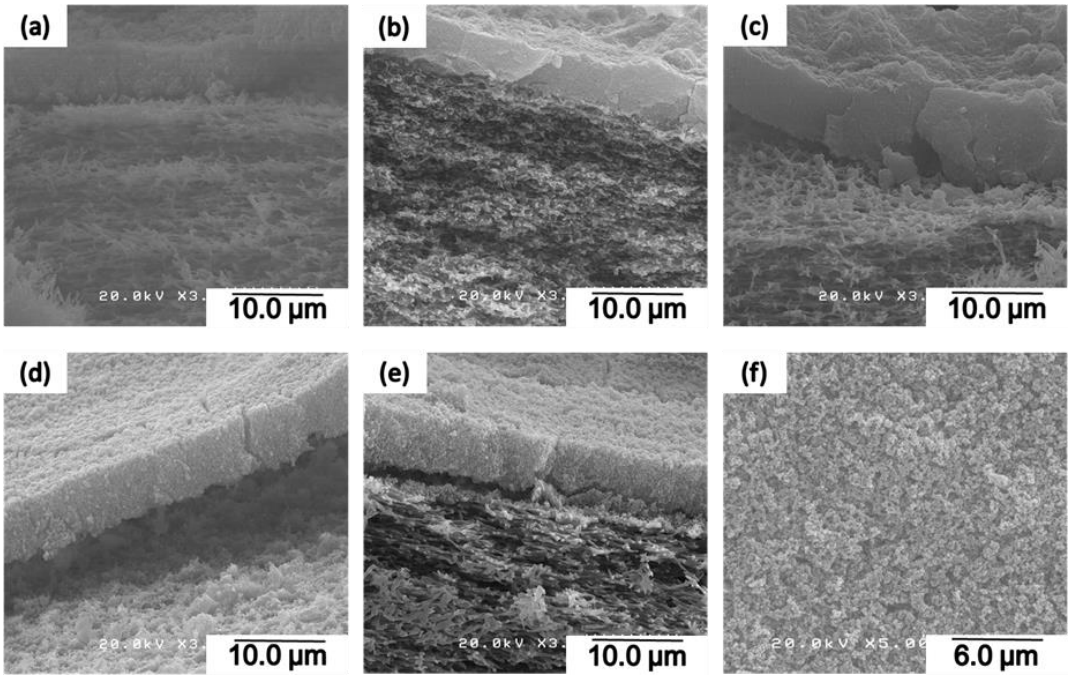

Figure 5. SEM images of UiO-66 membranes: cross-sectional images of a) UiO-66 (14 nm), b) UiO-66 (20 nm), c) UiO-66 (75 nm), d) UiO-66 (88 nm), and e) UiO-66 (108 nm), f) Top view image of UiO-66 (108 nm).

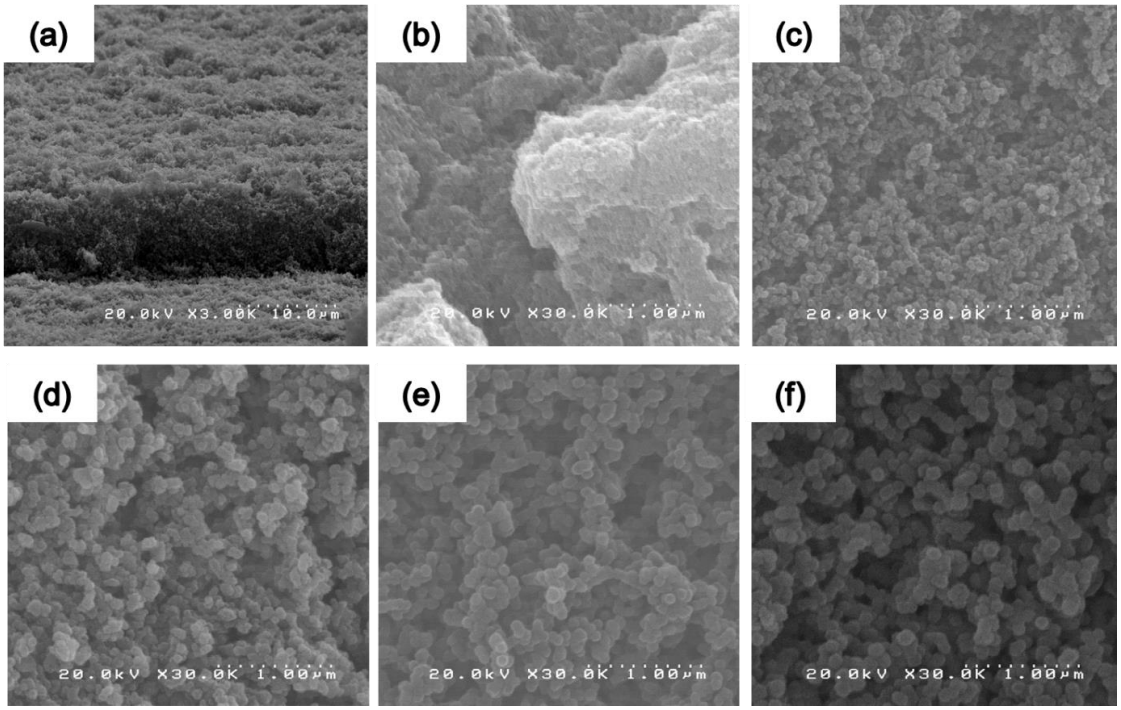

Figure 6. SEM image of the UiO-66 packing layer (cross-section): a) UiO-66 (14 nm), b) UiO-66 (20 nm), c) UiO-66 (23 nm), d) UiO-66 (75 nm), e) UiO-66 (88 nm) and f) UiO-66 (108 nm).

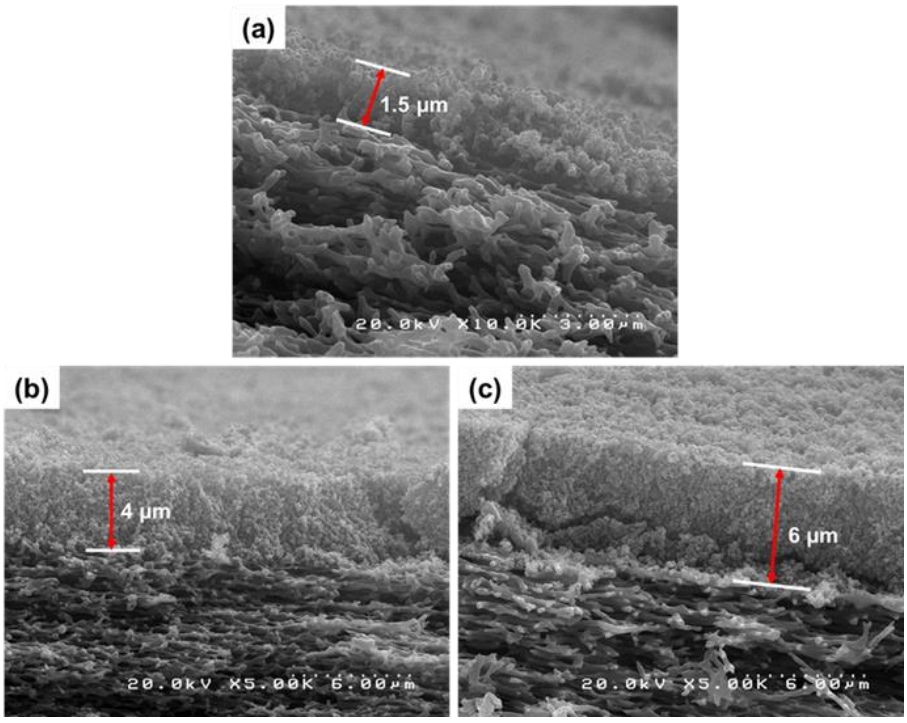

Figure 7. Cross-sectional SEM images of the UiO-66 (108 nm) composite membranes at different UiO-66 (108 nm) at loading: a) 1.0 mg, b) 3.0 mg, and c) 4.0 mg.

Filtration of Methylene Blue on the Bimodal Inorganic UiO-66 Nanocomposite

Nanochannel-based materials such as graphene oxide (GO) were reported to have a water flux of 428 L/m^2.h.bar whereas the cross-linked GO with isophorone diisocyanate (IPDI) membrane, which was supposed to enlarge nanochannels among GO sheets for higher water permeability, exhibited only a flux of 80–100 L/m^2.h.bar at supposedly extremely low external pressure (1.0 bar) with maximum rejection rate of 96% for dyes including methylene blue and methylene orange, respectively, which is comparatively lower in both water permeability and methylene blue rejection compared to MOFs membranes prepared in this work (Huang, H., et al., 2016; Hu, M., et al., 2019;). The abundant flow of nanochannels in the UiO-66 nanoparticles that form a selective layer primarily contributed to the high performance of the membranes. In addition, the incorporation of these porous nanoparticles into the substrate membrane could have introduced additional free volume between the UiO-66 nanoparticles and substrate matrix wrapping around the MOFs, leading to a significant increase in the water permeance without any loss of MB rejection, as well as interparticle voids, which could have insignificantly contributed to the permeability as reported in our earlier articles (Zhang, X., et al., 2014; Zheng, J., et al., 2015; Liu, J., et al., 2017). Interestingly, the UiO-66 (14 nm) membrane (smallest particle size) has the highest flux compared to its counterparts at 99 percent rejection, and the flux decreases as the size increases. This may be due to the nanopore sizes and free volume between the UiO-66 nanoparticles and substrate matrix. Nevertheless, regardless of these differences in permanence among the sizes, all the unimodal membranes prepared in this work exhibited higher permeate flux compared to other MOFs like MIL-101 (Cr) prepared by other techniques like Langmuir-Schaefer, whose flux was in the range of 7.5±0.7 to 7.7±1.1 L/m^2.h for crystal violet and 1.5±0.1 to 3.9±0.3 L/m^2.h for sunset yellow as reported by Echaide-Gorriz, et al., 2016; Navarro, et al., 2018) while the ZIF-8/PSS hybrid membrane prepared through layer-by-layer self-assembly recorded a water flux of 210 Lm^{-2}h^{-1} MPa^{-1} at 98.6% methyl blue rejection (Wang, et al., 2015). Furthermore, the segmented polymer networks fabricated by in-situ polymerization of synthesized multifunctional thin

selective layer on substrate membrane which have been reported to have recorded highest permeance of 45.6 L/m^2.h.bar for MB (Zhang, et al., 2018; Li, et al., 2018; Zuo, et al., 2019; Feng, et al., 2019) Comparatively, the least value of the permeance (380.35±23% L/m^2.h) of the UiO-66 membrane prepared in of our previous work (Trinh, et al., 2017; Goji, et al., 2018; outperformed the performances of the above-mentioned membrane by far and most of literature data (Ji et al., 2017: Qin et al., 2017; Goji, et al., 2018).

Figure 8 displays the filtration performance of UiO-66 (14 nm) and UiO-66 (108 nm) membranes with rejection of methylene blue as function of loading. The filtration performance of UiO-66 membranes with nanoparticle sizes of 14 nm and 108 nm was evaluated by measuring the rejection of methylene blue as a function of loading. Results indicated that both water permeability and methylene blue rejection decreased as the loading amount varied. Specifically, the UiO-66 (14 nm) membrane exhibited a flux of 350 ± 5.53 L/m²·h, while the UiO-66 (108 nm) membrane showed a flux of 300 ± 4.01 L/m²·h, both achieving 99% rejection of methylene blue. These differences in flux are attributed to size variations and the formation of large free volumes resulting from excess small-sized nanoparticles, leading to nonselective voids (Goji etal.,2018). In contrast, larger UiO-66 particles form a thicker layer on the substrate membrane without free volume, resulting in longer residence times for water passage and affecting methylene blue rejection(Fu et al., 2023)

References

Alghunaimi, F. A., Alomair, O. A., Al-Suhybani, A. A., & Naseem, R. (2018). Preparation, characterization, and performance evaluation of TiO_2-PANI nanocomposite membrane for wastewater treatment. *Separation and Purification Technology, 195*, 55-64.

Baker, R. W. (2012). *Membrane technology and applications*. John Wiley & Sons.

Chakrabarty, B., Saha, S., & Saha, B. (2018). Polymer-based membranes for pervaporation: A review on recent developments. *Journal of Applied Polymer Science, 135*(9), 45835.

Chen, Y., Zhang, J., Xiong, R., & Zhang, Y. (2018). Fabrication of chitosan/GO nanocomposite membrane for water treatment. *Carbohydrate Polymers, 190*, 19-26.

Ghosh, A. K., & Sarkar, A. K. (2018). A review on application of nanofiltration for water treatment. *Chemical Engineering Research and Design, 137*, 226-246.

Goh, P. S., Ismail, A. F., Sanip, S. M., & Ng, B. J. (2019). Nanofiltration membranes in water treatment: A review. *Desalination, 452*, 258-270.

Goji, S. Y., Chammingkwan, P., Dai, X. T., & Taniike, T. (2018). Design of a semi-continuous selective layer based on deposition of UiO-66 nanoparticles for nanofiltration. *Membranes, 8*, 129.

Huang, H., Xu, Y., Zhang, J., Chen, L., & Xu, N. (2021). Bimodal membrane based on UiO-66 nanoparticles: Enhanced separation performance via thermal annealing. *Journal of Membrane Science, 622*, 118967. https://doi.org/10.1016/j.memsci.2021.118967

Huang, J., Wang, X., Qiao, Z., Zhou, Y., Zhang, C., & Zhang, X. (2020). In-situ growth of UiO-66 nanocrystals in a polysulfone membrane for highly efficient separation. *Journal of Membrane Science, 612*, 118440. https://doi.org/10.1016/j.memsci.2020.118440

Jindal, A., Rana, D., & Matsuura, T. (2016). Nanofiltration: A membrane separation process for removal of emerging pollutants from water and wastewater. *Chemical Engineering Research and Design, 107*, 10-29.

Li, J., Du, X., Pan, S., Zhu, L., & Lu, Y. (2018). Preparation and characterization of carbon nanotube/polyvinylidene fluoride composite membranes for organic solvent nanofiltration. *Journal of Membrane Science, 546*, 149-157.

Li, Y., Li, L., & Li, G. (2018). Nanofiltration membranes: Synthesis, properties, and applications. *Chemical Engineering Science, 188*, 168-196.

Liu, Y., Gao, W., Li, L., & Chen, V. (2019). Preparation of bimodal nanocomposite membrane via ex-situ growth of UiO-66 nanoparticles on PVDF membrane for organic dye removal. *Journal of Colloid and Interface Science, 553*, 44-54. https://doi.org/10.1016/j.jcis.2019.05.073

Lueptow, R. M., & Khinast, J. G. (2017). *Membrane separation technology*. Springer International Publishing.

Ma, X., Ma, J., Gao, C., & Zhang, Y. (2020). Design and fabrication of nanocomposite membranes for water treatment. *Journal of Membrane Science, 611*, 118307.

Moghaddam, M., Behbahani, R. M., & Sadeghi, M. (2021). Preparation and characterization of bimodal UiO-66/PVDF nanocomposite membranes via ex-situ deposition for nanofiltration application. *Chemical Engineering Research and Design, 172*, 400-413. https://doi.org/10.1016/j.cherd.2021.06.017

Mondal, S., & Wickramasinghe, S. R. (2019). Nanofiltration: Principles, mechanisms, and applications. In *Nanotechnology in water and wastewater treatment* (pp. 39-65). Springer, Cham.

Nunes, S. P., & Peinemann, K. V. (2010). *Membrane technology in the chemical industry*. Wiley-VCH Verlag GmbH & Co. KGaA.

Rana, D., & Matsuura, T. (2010). Surface modifications for antifouling membranes. *Chemical Reviews, 110*(4), 2448-2471.

Su, Y., Li, Y., Li, L., Li, Y., & Li, G. (2020). Fabrication of high-performance bimodal nanocomposite membranes by incorporating UiO-66 nanocrystals for nanofiltration applications. *Separation and Purification Technology, 232*, 115915.

Sun, J., Wang, J., Yan, N., & Zhang, L. (2017). UiO-66-based composite membranes for molecular sieving and nanofiltration. *ACS Applied Materials & Interfaces, 9*(5), 4725-4733.

Teng, Z., Zhao, Y., & Tang, C. Y. (2018). Metal–organic framework-based membranes for water purification. *Current Opinion in Chemical Engineering, 19*, 92-103.

Van der Bruggen, B., & Vandecasteele, C. (2007). *Membrane technology: Applications and future directions*. CRC Press.

Wang, J., Zhang, M., & Li, X. (2019). Preparation of a bimodal nanocomposite membrane via the deposition of UiO-66 nanoparticles onto a polyethersulfone support membrane for nanofiltration. *Separation and Purification Technology, 211*, 575-584. https://doi.org/10.1016/j.seppur.2018.10.035

Wang, X., Li, Y., Li, L., & Li, G. (2021). Fabrication of bimodal UiO-66/GO nanocomposite membranes for nanofiltration and antibacterial applications. *Chemical Engineering Journal, 407*, 127254.

Wijmans, J. G., & Baker, R. W. (2012). Membrane technology: Recent advances and future directions. *Elsevier*.

Wu, H., Cai, X., Zhang, S., & Xie, S. (2019). The fabrication of polyamide/graphene oxide composite nanofiltration membranes with high flux and anti-fouling properties. *Journal of Membrane Science, 572*, 329-339.

Yang, Q., Huang, Y., Liu, J., Zhang, S., & Wang, J. (2019). Fabrication of graphene oxide modified thin-film nanocomposite membrane with improved seawater desalination performance. *Journal of Membrane Science, 584*, 162-173.

Yu, C., Zhang, X., Zheng, Y., Jiang, X., & Lu, Y. (2017). Effects of water and acid concentration on the morphology and size of UiO-66 crystals. *CrystEngComm, 19*, 2240-2245.

Zhang, M., & Li, Y. (2021). Bimodal nanocomposite membranes with UiO-66 nanoparticles for enhanced nanofiltration performance. *Journal of Membrane Science, 636*, 119475.

Zhang, X., Xue, Y., Wang, X., Li, J., Li, X., & Mulder, M. (2012). *Basic principles of membrane technology*. Springer Science & Business Media.

Zheng, F., Li, Y., Li, L., Chen, Y., Zhao, X., & Wang, S. (2019). Nanocomposite membranes with MXene nanosheets for water purification: A review. *Separation and Purification Technology, 222*, 191-202.